



UNIVERSITEIT•STELLENBOSCH•UNIVERSITY
jou kennisvenoot • your knowledge partner

Optimal design of a coreless stator axial field permanent magnet generator (repository copy)

Article:

Wang, R-J., Kamper, M.J., van der Westhuizen, K., Gieras, J.F., (2005) Optimal design of a coreless stator axial field permanent magnet generator, *IEEE Transactions on Magnetics*, 41(1): 55--64, January 2005; ISSN: 1941-0069

<http://dx.doi.org/10.1109/TMAG.2004.840183>

Reuse

Unless indicated otherwise, full text items are protected by copyright with all rights reserved. Archived content may only be used for academic research.

Optimal Design of a Coreless Stator Axial Flux Permanent-Magnet Generator

Rong-Jie Wang, *Member, IEEE*, Maarten J. Kamper, *Member, IEEE*, Kobus Van der Westhuizen, and Jacek F. Gieras, *Fellow, IEEE*

Abstract—This paper describes a hybrid method for calculating the performance of a coreless stator axial flux permanent-magnet (AFPM) generator. The method uses a combination of finite-element analysis and theoretical analysis. The method is then incorporated into a multidimensional optimization procedure to optimally design a large power coreless stator AFPM generator. The measured performance of the manufactured prototype compares favorably with the predicted results. The design approach can be applied successfully to optimize the design of the coreless stator AFPM machine.

Index Terms—Axial flux, design, finite-element methods, optimization methods, permanent-magnet generator.

I. INTRODUCTION

AXIAL FLUX permanent-magnet (AFPM) machines with coreless stators are regarded as high-efficiency machines for distributed power generation systems [6], [13], [19]. Because of the absence of core losses, a generator with this type of design can potentially operate at a higher efficiency than conventional machines. Besides, the high compactness and disk-shaped profile make this type of machine particularly suitable for mechanical integration with wind turbines and internal combustion engines (ICE), e.g., as integrated starter-generators.

A schematic drawing of a typical coreless stator AFPM machine is shown in Fig. 1. The machine consists of two outer rotor disks and one coreless stator in the middle. On the two opposing rotor disks, there are surface-mounted permanent magnets (PMs). The coreless stator winding consists of a number of single-layer trapezoidal-shaped coils. These coils have the advantages of being easy to make and having relatively short overhangs. The coils are held together and in position by using a composite material of epoxy resin and hardener.

So far, most published works regarding design optimization of AFPM machines have been limited to maximizing (minimizing) an objective function with respect to a *single* variable [3], [4], [9], [10], [15] using *analytical* methods. The finite-element method (FEM) is, in many instances, used merely to investigate certain design aspects. Since FE models give an excellent

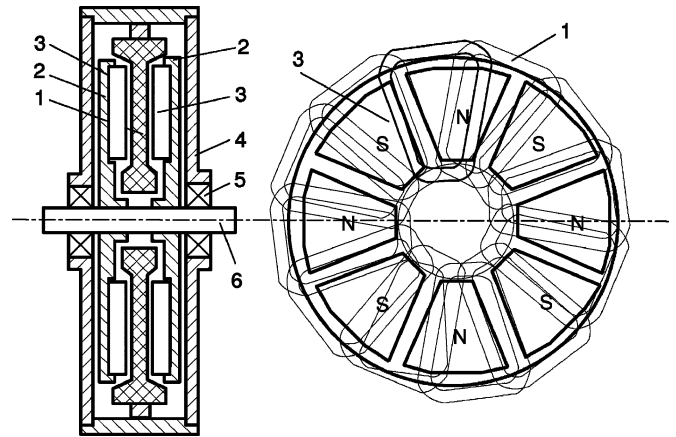


Fig. 1. Basic structure of the AFPM machine with a coreless stator. 1: Stator winding. 2: Steel rotor. 3: PMs. 4: Frame. 5: Bearing. 6: Shaft.

representation of the magnetic field inside the machine, enabling nonlinearity to be accounted for with great accuracy, it has been pointed out in the literature [5], [7], [20] that two-dimensional (2-D) FEM should be incorporated into design optimization of AFPM machines. However, there are no published works describing the implementation of this approach to the design of AFPM machines in detail.

In this paper, the equivalent circuits of a coreless AFPM generator are first established (Section II). The calculation of circuit parameters by using both FEM (Section III) and classical theory (Section IV) are then described. The performance calculation of the coreless stator AFPM generator is explained in Section V, which is then incorporated into a multidimensional optimization procedure to optimally design a large power coreless stator AFPM generator (Section VI). Some important mechanical design aspects are discussed in Section VII. The measured performance of the manufactured prototype are compared with the predicted results in Section IX. It is shown that the proposed design approach can be applied successfully to optimize the design of the coreless stator AFPM machine.

II. EQUIVALENT CIRCUITS

To calculate the performance of the AFPM machine, it is essential to consider the equivalent circuits of the machine. The fundamental per phase equivalent circuit of a coreless AFPM machine with the same reluctance for the magnetic flux in the d and q axis may be represented by the electric circuit shown in Fig. 2(a). In this circuit, R_s is the stator resistance, L_s is the stator inductance, e_m is the induced electromotive force (EMF) due to the fundamental air-gap PM flux linkage, and v_a and i_a

Manuscript received May 25, 2004; revised October 29, 2004. This work was supported by the University of Stellenbosch and SA industry.

R.-J. Wang and M. J. Kamper are with the Department of Electrical Engineering, University of Stellenbosch, Matieland 7602, South Africa (e-mail: rwang@sun.ac.za; kamper@sun.ac.za).

K. Van der Westhuizen is with the Department of Mechanical Engineering, University of Stellenbosch, Matieland 7602, South Africa (e-mail: kvdw@sun.ac.za).

J. F. Gieras is with the United Technologies Research Center, East Hartford, CT 06033 USA (e-mail: jgieras@utrc.utc.com).

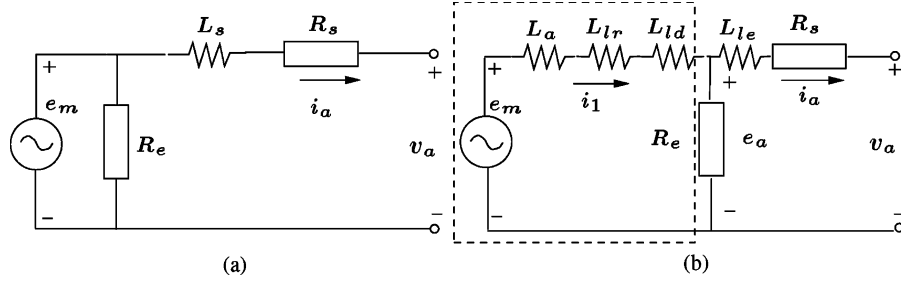


Fig. 2. Per-phase equivalent circuits of an AFPM machine.

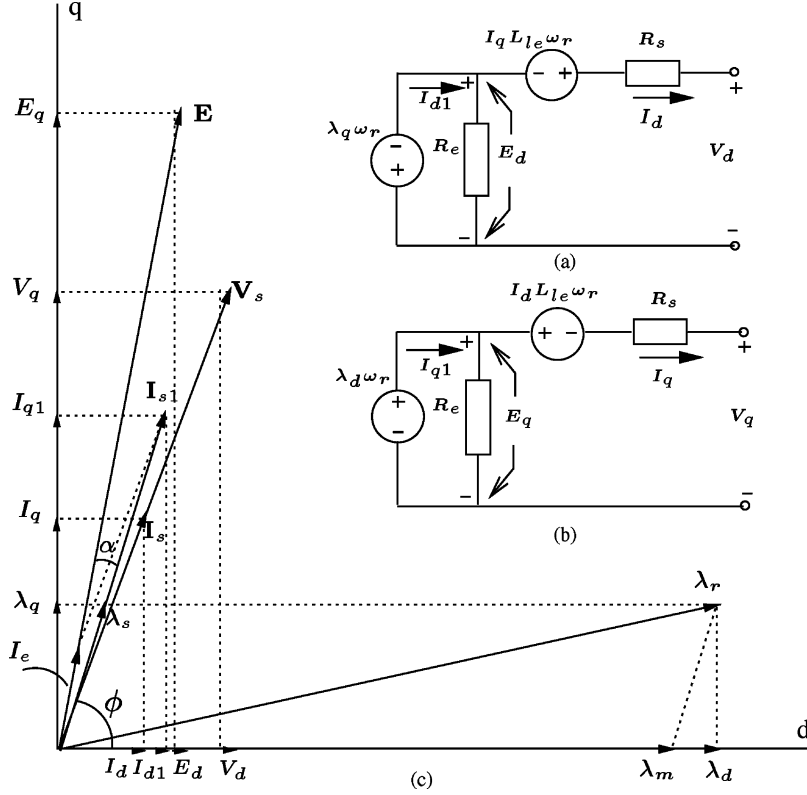


Fig. 3. d - and q -axis equivalent circuits and phasor diagram of the AFPM machine.

are the fundamental instantaneous phase voltage and current, respectively. The shunt resistance R_e is the stator eddy-current loss resistance.

The synchronous inductance L_s consists of the armature reaction (mutual) inductance L_a and the leakage inductance $L_l = L_{lr} + L_{ld} + L_{le}$ as shown in Fig. 2(b), where L_{lr} , L_{ld} , and L_{le} are leakage inductance, differential leakage inductance about the radial portion of conductors, and end winding leakage inductance, respectively. Unlike conventional slotted machines, there is no clear definition for main and leakage inductances in a coreless or slotless machine [1], [11], [17]. It is generally difficult to derive accurate analytical expressions for L_{lr} , L_{ld} , and L_{le} . With 2-D FE analysis, both mutual and leakage flux linkages can be readily taken into account. The only remaining part is the end-winding leakage flux. The synchronous inductance of the coreless machine may thus be split into two terms: 1) $L_a + L_{lr} + L_{ld}$ and 2) end connection leakage inductance L_{le} . As an approximation, R_e may be shifted to the left of L_{le} in the

equivalent circuit as shown in Fig. 2(b). In this way, the part of the equivalent circuit marked by the dotted lines in Fig. 2(b) can be accurately calculated by directly using FEM instead of approximate inductance equations.

The corresponding steady-state d - and q -axis equivalent circuits of the AFPM machine in the rotor reference frame are shown in Fig. 3. The flux linkages λ_d and λ_q are the d - and q -axis total stator flux linkage components. These flux linkages include the flux linkage due to the permanent magnets, λ_m , and the flux linkage due to stator currents, $\lambda_s = \lambda_a + \lambda_{lr} + \lambda_{ld}$, but exclude the end-winding flux linkage, λ_{le} . The parameter ω_r is the electrical speed of the rotor reference frame. In the phasor diagram (unity power factor was assumed), the space phasors \mathbf{V}_s and \mathbf{I}_s represent the stator terminal voltage and current, respectively. Note that \mathbf{I}_{s1} includes the equivalent eddy-current loss component \mathbf{I}_e . It has also been assumed that the eddy-current losses in the PMs and rotor disks are negligible.

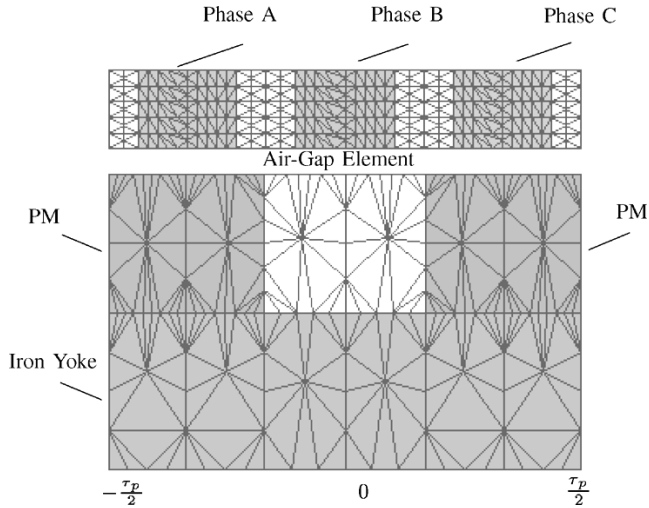


Fig. 4. 2-D FE model of a coreless stator AFPM machine.

III. CALCULATION OF EQUIVALENT CIRCUIT PARAMETERS USING FEM

This section describes how the equivalent circuit parameters of Fig. 3 are calculated by using FEM.

A. Finite-Element Model

The 2-D FE modeling of an AFPM machine is usually carried out by introducing a radial cutting plane at the average radius, which is then developed into a 2-D flat model. Owing to the symmetry of an AFPM machine, each half of the machine from the center plane mirrors the other half in axial direction. It is possible to model only half of the machine comprising the rotor disk, the air-gap clearance, and half of the stator. The air-gap region is modeled using the Cartesian air-gap element (CAGE), as described in [27]. By assigning negative periodic boundary conditions to the left and right boundaries, it is sufficient to model only one pole-pitch of the machine. Fig. 4 shows an FE mesh coupled with a CAGE for such a model, which spans one pole-pitch of the AFPM machine. For an AFPM machine with coreless stator, there is no tangential field component on the center plane of the stator so that the Neumann boundary condition can be assigned to the top boundary.

B. Calculation of Flux Linkages

To calculate the flux linkage using the FEM, it is necessary to specify the phase current $I = \hat{I} \angle \phi$ of the AFPM machine. The amplitude of the current space phasor \hat{I} may be determined from a given copper loss P_{cu} , which is predetermined based on the thermal analysis of the machine, by using

$$\hat{I} = \sqrt{\frac{2P_{cu}}{3R_s}} = I_q; \quad (I_d = 0) \quad (1)$$

in which a current angle of $\phi = 90^\circ$ has been assumed for balanced resistive load. With the I_d and I_q current component amplitudes known, the instantaneous three-phase currents i_{abc} , which need to be put in the FE program according to the rotor position, can be calculated using the inverse Park transformation. The defined FE model is solved by using a nonlinear solver

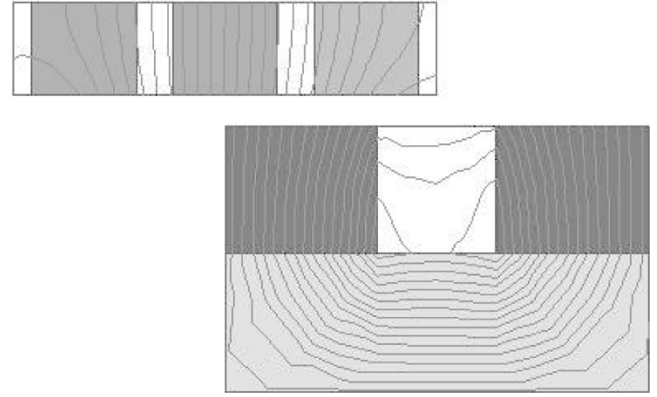


Fig. 5. Flux distribution in a coreless stator AFPM machine.

to obtain the nodal magnetic vector potentials of the model. Fig. 5 shows the flux plot of a coreless stator AFPM machine. The total three-phase flux linkages λ_{abc} , excluding end-winding flux linkages, are then computed in the FE program as follows [18]:

$$\lambda_{abc} = \frac{2pzl}{n_a S} \sum_{j=1}^u \left[\frac{\Delta_j \zeta}{3} \sum_{i=1}^3 A_{ij} \right]. \quad (2)$$

In (2), A_{ij} is the nodal value of the magnetic vector potential of the triangular element j , $\zeta = +1$ or $\zeta = -1$ indicates the direction of integration either into the plane or out of the plane, Δ_j is the area of the triangular element j , u is the total number of elements of the meshed coil areas of the phase in the pole region, n_a is the number of parallel circuits (current paths) per phase, n is the total number of elements of the in-going and out-going areas of the coil, z , l and S are the number of turns, length, and area of a coil, respectively.

From a machine design perspective, it is of main interest to find the fundamental components of the total flux linkages. For a coreless stator AFPM machine, the flux linkage harmonics due to iron stator slots and magnetic saturation are absent. Owing to a large air gap, the harmonics caused by stator winding MMF space distribution are negligible. The most important flux linkage harmonics needed to account for are those due to the flat-shaped PMs.

Given these considerations, the flux linkage wave of an AFPM machine is nearly sinusoidal, though, for a nondistributed winding, an appreciable third and less significant fifth and seventh harmonics are still present in the total flux linkage waveform. If the fifth, seventh, and higher harmonics are ignored, the fundamental total phase flux linkages can be calculated by using the technique given in [18], i.e.,

$$[\lambda_{abc1}] \approx [\lambda_{abc}] - [\lambda_{abc3}] \quad (3)$$

where the co-phasal third-harmonic flux linkage, including the higher order triple harmonics, can be obtained from

$$\lambda_{a3} = \lambda_{b3} = \lambda_{c3} \approx \frac{1}{3}(\lambda_a + \lambda_b + \lambda_c). \quad (4)$$

The use of (3) and (4) is of great importance in the optimization process as it enables the fundamental total phase flux linkages of the AFPM machine to be determined by using just one

set of field solutions. The fundamental flux linkages are the basis of subsequent performance calculation of the machine.

With the fundamental total phase flux linkages and rotor position known, the dq flux linkages are calculated using Park's transformation as follows [12]:

$$[\lambda_{dqo}] = [K_p][\lambda_{abc1}] \quad (5)$$

where

$$K_p = \frac{2}{3} \begin{bmatrix} \cos \theta & \cos \left(\theta - \frac{2\pi}{3} \right) & \cos \left(\theta + \frac{2\pi}{3} \right) \\ -\sin \theta & -\sin \left(\theta - \frac{2\pi}{3} \right) & -\sin \left(\theta + \frac{2\pi}{3} \right) \\ \frac{1}{2} & \frac{1}{2} & \frac{1}{2} \end{bmatrix}. \quad (6)$$

From this, the speed dependent voltages $E_d = -\lambda_q \omega_r$ and $E_q = \lambda_d \omega_r$ of the equivalent circuits are determined.

IV. EQUIVALENT CIRCUIT PARAMETERS CALCULATED BY CLASSICAL THEORY

In this section, the calculation of the remaining equivalent circuit parameters of Fig. 3 such as winding resistance, eddy-current resistance, and end-winding inductance by using classical theory is described.

A. Stator Winding Resistance

The temperature-dependent stator winding resistance per phase R_s is calculated as

$$R_s = \frac{2n_t(l + l_e)}{\sigma_T n_a s_{cu}} \quad (7)$$

where n_t is the number of turns in series per phase, σ_T is the electric conductivity of the wire at temperature T , and s_{cu} is the cross section area of the wire. The skin effect has not been taken into account in (7) as thin parallel wires (0.42 mm diameter) were used to minimize this effect in the design.

B. Eddy-Current Resistance

For an AFPM machine with a coreless stator, associated iron losses are absent. The core losses in the ferromagnetic rotor disks (back irons) are also negligible due to low flux variation. However, the eddy-current losses in the stator winding are significant due to the high pole number rotor that may spin at relatively high speeds. The shunt resistance R_e may be calculated in the same way as that of the core loss resistance described in [16], [18] to account for the eddy-current losses, i.e.,

$$R_e = \frac{3E_a^2}{P_e} \quad (8)$$

where E_a is the rms value of phase EMF (see Figs. 2 and 3) and is given by

$$E_a = \sqrt{\frac{E_d^2 + E_q^2}{2}}. \quad (9)$$

A detailed treatment of the calculation of eddy-current losses in AFPM machine has been given in [24]. As an approximation, one may consider only the eddy-current losses due to the

main flux and fundamental operating frequency of the machine. The eddy-current losses (for round conductors) are calculated by using [8]

$$P_e = \frac{\pi l d^4 \omega^2}{32\rho} (B_x^2 + B_y^2) N_c \quad (10)$$

where $l \approx r_o - r_i$ is the conductor length, ω is the fundamental frequency, d is the diameter of the conductor, N_c is the total number of conductors in the machine, and B_x and B_y are the peripheral and axial components (peak values) of the fundamental flux density wave, respectively. The values of the flux density components can be obtained from the FE field solution.

C. End-Winding Inductance

The end-winding inductance L_{le} is calculated by using an analytical approach based on

$$L_{le} = 2\mu_0 \frac{n_t^2 l_e}{p q_1} P_{le} \quad (11)$$

where p is the number of pole pairs, q_1 is the number of coils per pole per phase, l_e is the length of the single-sided end connection, and P_{le} can roughly be estimated from the following semianalytical equation [14]:

$$P_{le} \approx 0.3q_1. \quad (12)$$

V. PERFORMANCE CALCULATION

From the dq current components and the end-winding leakage inductance L_e , the end-winding leakage flux linkage speed dependent voltages $L_e I_q \omega_r$ and $L_e I_d \omega_r$ of Fig. 3 are determined. The dq terminal voltage components, V_d and V_q , and the voltage amplitude V_s are calculated from

$$\begin{cases} V_d = E_d + L_{le} I_q \omega_r - I_d R_s \\ V_q = E_q - L_{le} I_d \omega_r - I_q R_s \\ V_s = \sqrt{V_d^2 + V_q^2} \end{cases}. \quad (13)$$

The power factor is easily calculated from the dq voltage components, V_d and V_q , and dq current components, I_d and I_q , as follows:

$$pf = \cos \left[\tan^{-1} \left(\frac{V_d}{V_q} \right) \pm \tan^{-1} \left(\frac{I_d}{I_q} \right) \right]. \quad (14)$$

The generated kVA of the machine is calculated as

$$S = \frac{3}{2} V_s I_s = \frac{3}{2} (V_d I_d + V_q I_q). \quad (15)$$

The steady-state electromagnetic torque of the AFPM machine can be calculated by using the following relation:

$$T_e = \frac{3}{2} p (\lambda_d \cdot I_{q1} - \lambda_q \cdot I_{d1}) = \frac{3}{2} p \lambda_m I_{q1}. \quad (16)$$

The total input shaft power of the generator can then be calculated by

$$P_{in} = \omega_r \cdot T_e + P_{wf} \quad (17)$$

where ω_r is the angular speed of the machine, and P_{wf} are the windage and friction losses, which can be estimated from [23]

$$P_{wf} = \frac{1}{2} c_f \rho (\pi n)^3 (D_o^5 - D_i^5) \quad (18)$$

where n is the rotation speed in revolutions per second (r/s), c_f is the friction coefficient, and ρ is the density of cooling medium. The active output power is calculated by using $P_{out} = S \times pf$. The efficiency is then given by $\eta = P_{out}/P_{in}$.

This concludes the calculation of the equivalent circuit and performance parameters of the AFPM machine. This calculation method is used by the optimization algorithm described in the next section.

VI. OPTIMIZATION

This section describes the design optimization of the AFPM machine. The aim of the optimization procedure is to minimize the amount of PM material used or maximize the efficiency of the machine, while ensuring a rated output power, acceptable current density, and desired phase voltage.

A. Optimization Algorithms

Two different optimization algorithms, i.e., Powell's method and the population-based incremental learning (PBIL) algorithm, are used in this paper for the unconstrained design optimization of the AFPM machine. The reasons for using these methods are:

- to compare the effectiveness of the linear maximization (minimization) method (Powell's method) with that of a stochastic method (PBIL);
- to verify the optimum design results by using two completely different algorithms.

1) *Powell's Method*: Powell's method is basically an iterative method. Each r th iteration of the procedure maximizes (minimizes) the objective function along n linearly independent directions, L_1, L_2, \dots, L_n . The initial set of n vector directions are the coordinate directions. After each iteration, a new direction is defined which is used to form the vector directions for the next iteration. After n iterations, a set of n mutually conjugate vector directions are obtained so that the maximum (minimum) of a quadratic function is found.

To avoid linear dependence and premature termination in the optimization, specially designed tests have been incorporated into the algorithm. A detailed explanation of this method is given in [18] and [22].

2) *PBIL Algorithm*: PBIL is a method combining genetic algorithms (GA) and competitive learning for function optimization [2], [14]. The algorithm attempts to generate a probability vector, which is then sampled to produce the next generation's population. Unlike GAs, operations of PBIL act directly on the probability vector instead of population. To maintain the most diversity, each bit position of the probabilities is set to 0.5 at the beginning. A number of solution vectors are generated based on the probabilities of the probability vector. The probability vector moves toward the solution vector with the highest eval-

uation. Each bit of the probability vector is updated based on update rule of competitive learning, i.e.,

$$p_i = p_i \times (1.0 - lr) + lr \times v_i \quad (19)$$

where p_i is the probability of generating a one in the bit position i , v_i is the i th position in the solution vector that the probability vector is being pushed toward, and lr is the learning rate, which is the amount the probability vector is changed after each cycle. The learning rate has a significant effect on the convergence speed.

After each update of the probability vector, a new set of solution vectors is created. As the search progresses, the values in the probability vector start to move toward either 0 or 1 representing a high evaluation solution vector. The use of *mutation* in PBIL is for the same reason as in the GA, i.e., to prevent premature convergence.

3) *Constrained Optimization*: To transform constrained optimization problems into unconstrained ones, the penalty function is used together with Powell's method. The objective function is modified by adding terms or functions that penalize any increased constraint violation. The resultant objective function is then

$$F(\vec{x}, w) = f(\vec{x}) + \sum_{i=1}^u w_i \epsilon_i(\vec{x}) \quad (20)$$

where $f(\vec{x})$ is the function to be minimized, w_i are weighting factors, and $\epsilon_i(x)$ are functions which penalize increased constraint violation.

Owing to the nature of the stochastic search, PBIL algorithms do not require the use of penalty functions in the objective functions.

B. Variables

The geometric layout of an AFPM machine with a coreless stator is shown in Fig. 6. Only five variables of the machine are selected. These are the PM thickness h_m , magnet width to pole pitch ratio τ_m/τ_p , stator winding thickness h_s , rotor disk inner radius r_i , and the air-gap clearance g . For the specific application, the rotor outer radius r_o is limited to 360 mm and the typical operating speed is about 2000 rpm. The number of parallel circuits per phase $n_a = 20$ and the number of poles $p = 40$ are predefined. The comparison done in previous studies [21] reveals that the design of an AFPM machine using purely electromagnetic calculations without taking into account mechanical strength requirements may lead to an unrealistically thin rotor disk. To rectify this problem, mechanical strength analysis is of great importance in determining the thickness of the rotor disk h_r . The FE analysis of the mechanical strength of the rotor disks is described later.

C. Objective Functions

The copper losses are kept constant in the design optimization program. An iterative procedure, making use of the thermo-fluid model established in [25], has been used to determine the maximum allowable losses that the machine can handle. The estimated allowable full-load copper loss is about 2.5 kW for a rated

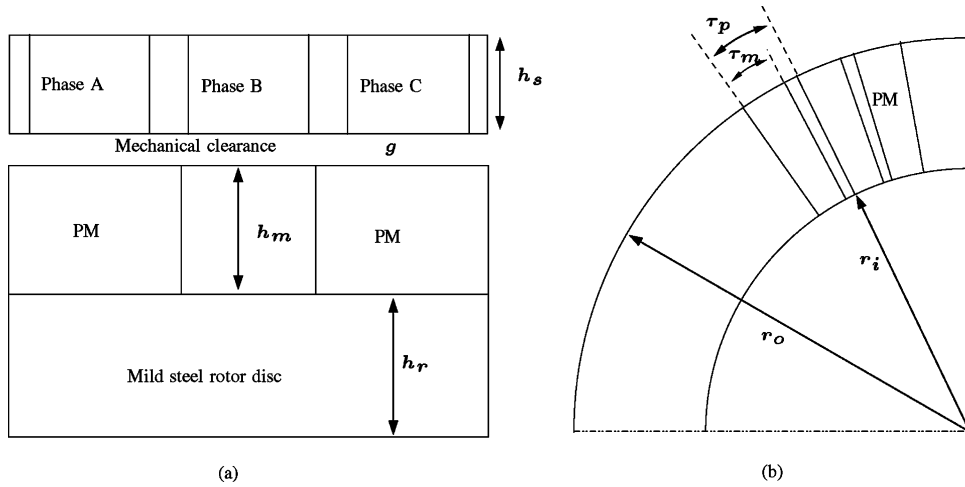


Fig. 6. Geometric layout of AFPM machine showing design variables: (a) a linearized section of the radial cutting plan, and (b) a rotor disk with PMs.

power of 150 kW [26]. The maximum allowable current density is set to 10 A/mm² in the design program. It has been confirmed experimentally that the AFPM machine can withstand this current density. The performance parameters to be optimized have been selected as the mass of the PM material and the efficiency.

1) *Optimize for Minimal Mass of PM Material:* The optimization problem for minimizing the total mass of the PM material, W_m , can be expressed as $\text{MIN}[W_m]$ subject to the following constraints:

$$\begin{cases} P_{\text{out}}(\vec{x}) \geq P_o \\ J(\vec{x}) \leq J_a \\ V_{ph}(\vec{x}) \leq V_a \end{cases} \quad (21)$$

where W_m is the total mass of the PM material used, P_o is the desired output power, J_a is the maximum allowed current density, and V_a is the maximum rms phase voltage at rated output power. This criterion is almost equivalent with the minimization of cost as PMs are expensive parts in a machine.

2) *Optimize for Maximum Efficiency:* The optimization problem for maximizing the machine's efficiency, η , can be expressed as $\text{MAX}[\eta]$ subject to the constraints

$$\begin{cases} P_{\text{out}}(\vec{x}) \geq P_o \\ J(\vec{x}) \leq J_a \\ V_{ph}(\vec{x}) \leq V_a \\ W_m(\vec{x}) \leq W_m \end{cases} \quad (22)$$

where η is the machine's efficiency at rated output power, P_o , and W_m is the maximum allowable mass of the PM material used at P_o .

D. Optimization Procedure

The overall design methodology presented in the paper is to use a combination of the classical circuit model and FE field solutions directly in a multidimensional optimization procedure. The basic structure of the approach is shown in Fig. 7. The optimization algorithm searches for the machine variables $[X]$ that minimizes (maximizes) the function value $F[X]$. In each iteration, a new FE mesh is generated according to machine dimension input $[X]$, a nonlinear solver is called to find the magnetic

vector potentials. The machine performance parameters $F[X]$ are calculated using flux linkages and circuit equations in post-processing as described in Section III.

Powell's method requires an initial value for each of the variables. If it is too far from the real optimum, then the optimization may end up being trapped in a local optimum in the vicinity of the initial value [28], which will lead to the necessity of testing with different sets of starting values to verify the optimum point.

When the PBIL algorithm is used, it does not really matter what starting values are used. A total of 30 sample bits, 6 bits per independent variable, were used in the optimization. The step sizes for the variables are 0.05 mm for the air-gap g , 0.01 mm for the PM height h_m , 0.1 mm for the stator thickness, 0.5 mm for the rotor inner radius r_i , and 0.005 for the PM width to pole pitch ratio. The number of bits and step size per variable were chosen to ensure the largest feasible range. The stopping rule of the PBIL algorithm is that the optimization cycles have to reach a preset number of generations.

During the optimization process, the mesh of the FE model changes as the optimization progresses. Occasionally, some of the elements may be badly shaped or ill conditioned resulting in poor accuracy or even no solution. It is therefore necessary to check that the model dimensions are reasonable before the FE mesh is constructed. A thermo-fluid model described in [25] is also incorporated in the optimization process to predict the temperature distribution in various parts of the machine and to thus check the validity of the design.

E. Results of the Optimized AFPM Machine

Starting from the same initial design, the optimization was done using both Powell's method and the PBIL algorithm according to the two different design objectives, i.e., maximum efficiency or minimum PM material, respectively. A comparison of the effectiveness between the two methods was also done. Table I shows the results of a maximum efficiency machine design of a 150 kW machine. Both optimization algorithms give similar results. For the design of minimum PM material (Table II), the PBIL optimization came up with a design using less PM material. It can be seen that Powell's method requires a total of 106 field solutions while the PBIL algorithm

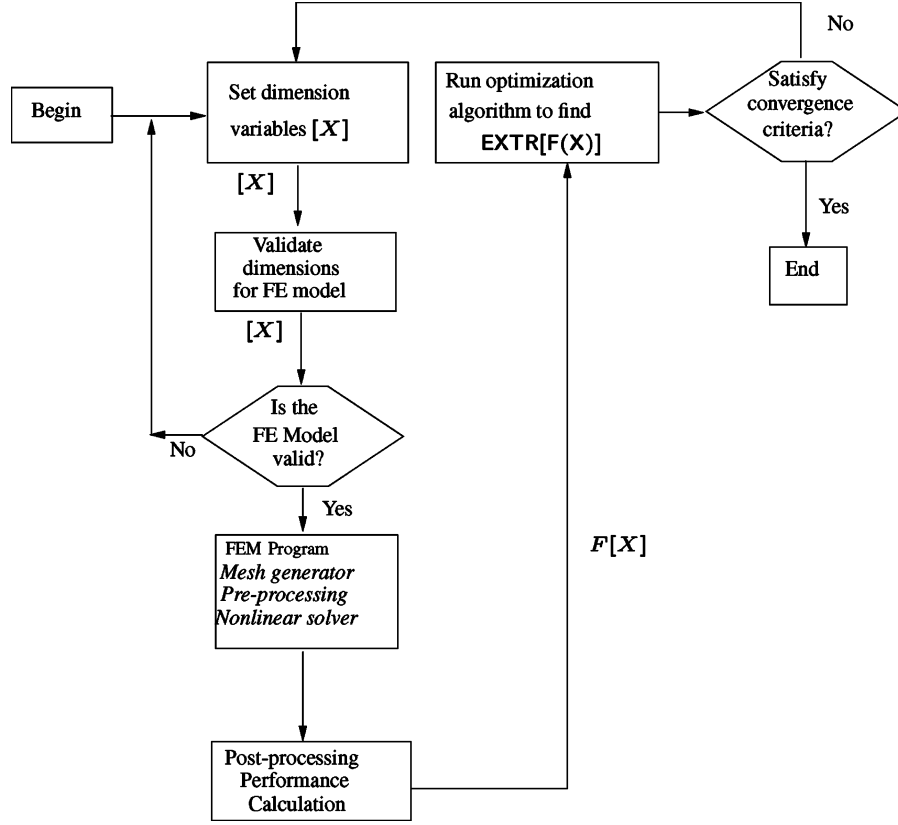


Fig. 7. Basic structure of the optimization procedure.

TABLE I
OPTIMIZATION RESULTS FOR MAXIMUM EFFICIENCY

Objective functions \Rightarrow	MAX[F(\vec{x})] ; $F(\vec{x}) = \eta\%$	
Variables [\vec{x}] \downarrow	Powell	PBIL
PM height (mm)	11.12	11.1
PM width/pole pitch	0.78	0.72
Stator thickness (mm)	17.5	15.6
Air-gap clearance (mm)	2.5	2.745
Rotor inner diameter (mm)	490.3	495
$F(\vec{x}) = \eta\%$	95.7%	95.8%
CPU time (Minutes) \Rightarrow	3.1	134
Number of solutions:	93	4522

TABLE II
OPTIMIZATION RESULTS FOR MINIMUM PM MATERIAL

Objective functions \Rightarrow	MIN[F(\vec{x})] ; $F(\vec{x}) = W_m$	
Variables [\vec{x}] \downarrow	Powell	PBIL
PM height (mm)	10.7	10.5
PM width/pole pitch	0.72	0.72
Stator thickness (mm)	15.7	16.3
Air-gap clearance (mm)	2.75	2.75
Rotor inner diameter (mm)	499.6	506
$F(\vec{x}) = W_m$	24.2 kg	23.2 kg
CPU time (Minutes) \Rightarrow	3.5	165
Number of solutions:	106	5562

needs 5562 field solutions. Obviously, Powell's method is a lot more efficient than the PBIL algorithm as it used only a fraction of the CPU time that the PBIL required. The design optimization was carried out on a 1670-MHz Intel PC running RedHat Linux operating system. On average it takes less than 2 s to solve one field solution.

TABLE III
PERFORMANCES OF DIFFERENT FE OPTIMIZED DESIGNS

Objective function		MAX [$\eta\%$]	MIN [W_m]		
Parameter	Cond.	Powell	PBIL	Powell	PBIL
P_o (kW)	≥ 150	174	164	159	154
J (A/mm^2)	≤ 10	6.86	7.12	7.08	6.84
$K_r = r_i/r_o$	-	0.681	0.688	0.694	0.703
V_{ph} (V)	≤ 300	283.5	254.8	251.5	248.8
I_{ph} (A)	-	208	217.1	215	210
pf	-	0.997	0.998	0.997	0.997
$\eta\%$	-	95.7	95.8	95.6	95.6
W_m (kg)	-	29.8	25.6	24.2	23.2
Design options		A	B	C	D

The calculated performances of the above optimized designs are shown in Table III. It was found that the inner to outer diameter ratio K_r is about 0.68 for the maximum efficiency design and around 0.7 for minimum PM mass and/or volume design. By minimizing the PM material, the cost and the mass of the machine are also reduced.

VII. MECHANICAL STRENGTH ANALYSIS

The deflection of the rotor disks due to the strong magnetic pull may have undesirable effects on an AFPM machine such as: 1) closing the running clearance between the rotor disk and the stator; 2) breaking the permanent magnets due to bending; 3) reducing air-flow discharging area, hence deteriorating the cooling capacity; and 4) a nonuniform air gap causing a drift in the electrical performance from the optimum. Besides, the rotor disks account for roughly 50% of the total active mass of an AFPM machine. Hence, the optimal design of the rotor disks is

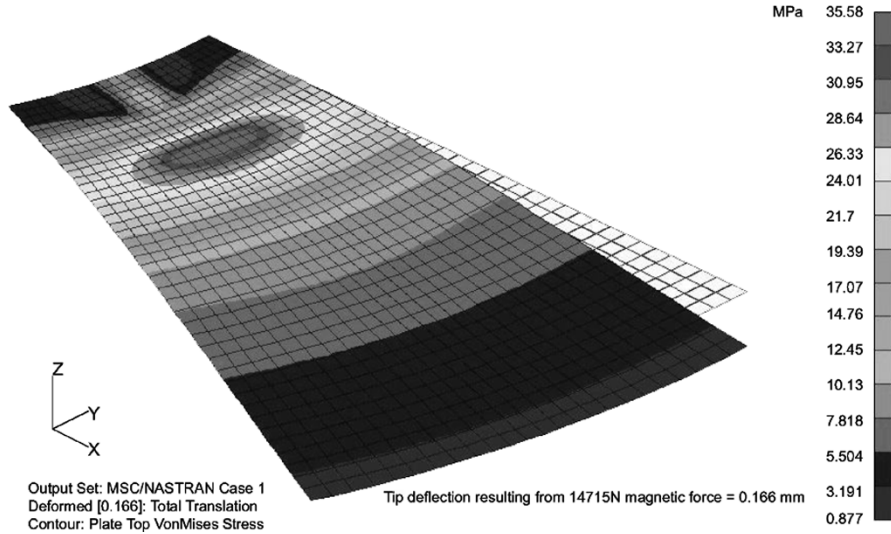


Fig. 8. Deflection (blown up) and Von Mises stress distribution of a rotor disk.

of great importance to realize a design of high power-to-mass ratio. All these aspects make the mechanical stress analysis of the rotor disk a necessity.

A. Mechanical Stress Analysis of Rotor Disk

The structure of the rotor disks of the designed AFPM machine was analyzed with the aid of an FEM structural program. The aim was to find a least thickness for the rotor disk, which satisfies the critical strength requirements of a rotor disk. The maximum tolerable deflection of the rotor disk was set to be 0.3 mm. This is to ensure that the PMs would not suffer any excessive forces that have the potential to break the magnets or peel them off from the steel disk.

By taking into account the symmetry of the machine, only one sixteenth of the rotor disk was analyzed using 4-node shell-elements, with symmetrical boundary conditions applied. The axial magnetic pull between PM disks at zero current state was calculated as 14.7 kN while the magnetic pull between the PM disk and stator under load due to tangential flux is rather insignificant (about 45 N). In the FE program, the magnetic pull-force is applied in the form of a constant 69.8 kPa pressure load over the total area that the PMs occupy. The stiffness provided by the magnets was not included so as to keep the design on the conservative side.

Based on the analysis, the rotor disk thickness was chosen as 17 mm with a maximum deflection of 0.145 mm. Fig. 8 shows the deflection (blown up) and the Von Mises stress distribution of the laboratory prototype 17 mm disk. The maximum stress of 35.6 MPa is much lower than the typical yield strength of mild steel that is in the region of 300 MPa. Previous studies [21] show that the bending of the rotor disk decreases toward its outer periphery. The rotor disk may be machined in such a way that the disk becomes thinner toward the outer periphery. As shown in Table IV, the tapered disk uses approximately 10% less iron than the straight disk. The maximum deflection increases by only 0.021 mm with the tapered disk, which is negligible. This can effectively save the active mass of the machine without compromising the mechanical strength. However, if manufacturing

TABLE IV
COMPARISON OF DIFFERENT DESIGNS OF ROTOR DISK

Parameter	Straight disk	Tapered disk
Mass (kg)	39.184	31.296
Max. Deflection (mm)	0.145	0.166
Max. Stress (MPa)	35.6	33.4

costs are taken into account for small production volumes, it is justifiable to use a steel disk with uniform thickness. The constructed machine described in the next section uses 17 mm straight disks.

VIII. PROTOTYPE MACHINE

To verify the optimization design and performance described in Section VI, an AFPM machine optimized for minimal PM material (design option C in Table III) has been built. Fig. 9 shows the constructed air-cooled coreless stator AFPM machine. The single stator is mounted on one side of the external frame. There are 20 parallel connected coils per phase, as shown in Table V. To facilitate making connections, four circular bus-bars are used as shown in Fig. 9(b). Rare-earth sintered NdFeB magnets are used, which has a remanent flux density (B_r) of 1.18 T and a maximum allowable working temperature around 130 °C. The hub structure shown in Fig. 9(c) serves as both air intake and supporting structure for the rotor disks. Furthermore, it also acts as a centrifugal fan improving the air cooling of the AFPM machine.

IX. PERFORMANCE

The performance tests on the prototype AFPM machine were carried out in the laboratory and were analyzed. The tests focused on its generation mode. A reconfigurable water-cooled bank of resistors was configured into a balanced three-phase load and then connected across the AFPM machine terminals. An induction machine was used as prime mover. The water cooling system consists of a water tank, pipe system, and a

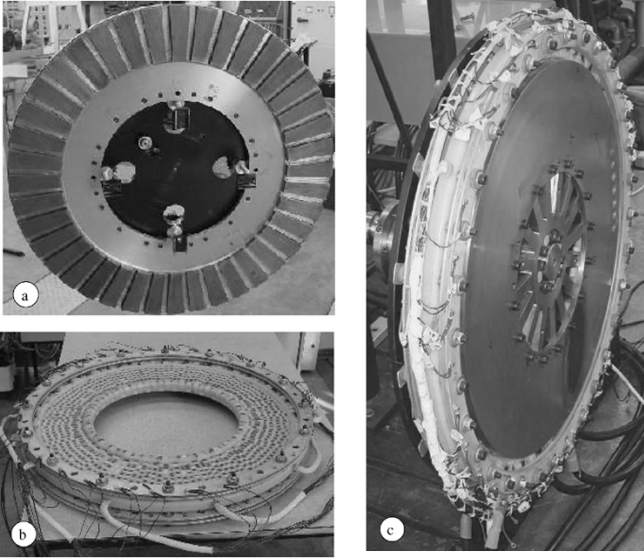


Fig. 9. The designed single-stage synchronous AFPM machine: (a) rotor disk with surface mounted PM segments, (b) coreless stator with busbars, and (c) the assembled machine.

TABLE V
DESIGN DATA FOR THE AFPM MACHINE UNDER STUDY

Rated line voltage	435 V (Star connection)
Rated phase current	215 A
Number of poles	40
Rated speed	1950 rpm
Axial length	72 mm
Outer diameter	720 mm
Inner diameter	500 mm
Magnet shape	Trapezoidal
Pole arc/pole pitch	0.72
Air-gap clearance	2.75 mm
Number of coils	60
Type of winding	Single layer trapezoidal
Turns per coil	51
Connection	20 parallel circuits/phase
Conductor	12 parallel wires/coil (twisted)
Conductor size	0.42 mm

cooling tower of 250 kW capacity. The testing setup is shown in Fig. 10.

In Fig. 11, the no-load phase voltage of the prototype machine at rated speed calculated by a FE time-stepped model is compared with the measured results. The details of the time-step modeling of AFPM machine is given in [27]. The output power and phase current were measured at different rotating speeds. The same conditions were simulated using the FE computer program. The load resistance value used in the computation under various load conditions was compensated with an estimated temperature factor. The results are presented and compared in Fig. 12. Agreement between measured and predicted output power and phase current is shown to be well within the limits of experimental accuracy.

As shown in Table VI, the rated output power of the AFPM generator at unity power factor is measured to be 154 kW at rated speed. Taking into account the mechanical loss (measured), eddy-current loss (measured), and copper loss (calculated), the total mechanical input power (ignoring the losses in PMs and rotor disks) is then 161 kW. This gives a machine efficiency of 95.7% at that speed. The total losses are

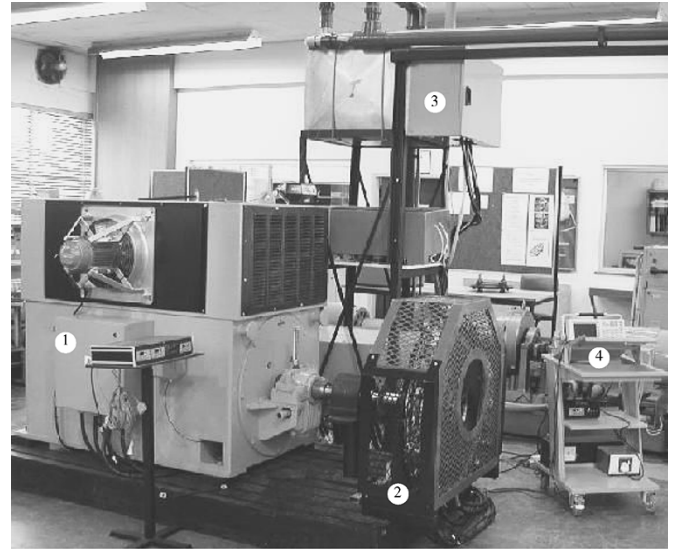


Fig. 10. Testing setup of the designed AFPM machine. 1: 600 kW induction machine drive. 2: AFPM generator. 3: Water-cooled resistive load. 4: Measuring equipment.

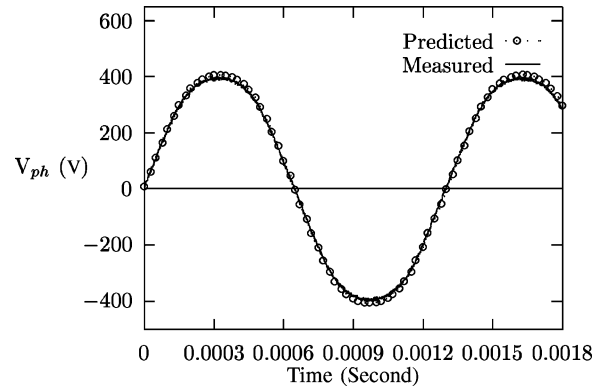


Fig. 11. Comparison of predicted and measured no-load phase voltages (2300 rpm).

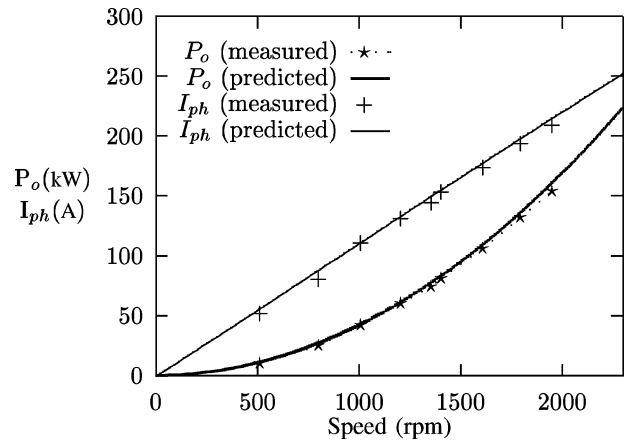


Fig. 12. Predicted and measured power and phase current for balanced three-phase operation.

6989.7 W, of which 1732 W are eddy-current losses, 3509 W are mechanical losses, and 1748.7 W are copper losses. The stabilized machine winding temperature rise was measured as 56 °C, which is not high and shows the good air cooling

TABLE VI
MEASURED PERFORMANCE AT RATED OPERATING CONDITION

Output power	154 kW
Input power	161 kW
Efficiency	95.7%
Eddy current losses	1732 W
Copper losses	1748.7 W
Mechanical losses	3509 W
Stabilized stator temperature (rated)	56°C

capacity in an essentially self-cooled AFPM generator. For an ambient temperature of 30 °C–40 °C, typical for ICE power generation applications, the actual temperature of the stator winding will be in the range of 86 °C–96 °C. The relatively high mechanical losses are mainly due to the windage losses. The power density of the machine is calculated as 4.43 MW/m³, which is relatively high when compared with that of conventional ac machines (typically 2.2–2.6 MW/m³).

X. CONCLUSION

The overall design methodology presented in the paper is to use a combination of classical circuit analysis and FE field analysis in an optimization process. Both Powell's method and the PBIL algorithm have been applied in the optimization process of the AFPM machine. Powell's method is more efficient than the PBIL algorithm as it needed only a fraction of the CPU time that the PBIL required. However, the PBIL optimization found slightly better solutions in all the case studies. By minimizing the PM material, an overall better design can be obtained with lower eddy-current losses, high efficiency, high power-to-mass ratio, and low cost.

One of the designed AFPM machines was built and tested. Owing to a very low phase inductance in the coreless stator AFPM machine, the output voltage varied almost linearly with the load current. When operated with a balanced three-phase resistive loading, the waveform of the stator phase voltage and current were found to be very close to sinusoidal. The measured performance of the prototype AFPM machine compares favorably with the predicted one.

REFERENCES

- [1] K. Atallah, Z. Q. Zhu, D. Howe, and T. S. Birch, "Armature reaction field and winding inductances of slotless permanent-magnet brushless machines," *IEEE Trans. Magn.*, vol. 34, no. 5, pp. 3737–3744, Sep. 1998.
- [2] S. Baluja, "Population-based incremental learning: A method for integrating genetic search based function optimization and competitive learning," Carnegie Mellon Univ., Pittsburgh, PA, Tech. Rep. CMU-CS-94-163, June 1994.
- [3] P. Campbell, "Principle of a PM axial field DC machine," *Proc. Inst. Elect. Eng.*, vol. 121, no. 1, pp. 1489–1494, 1974.
- [4] F. Caricchi, F. Crescimbin, A. D. Napoli, and E. Santini, "Optimum CAD-CAE design of axial flux permanent magnet motors," in *Proc. IECM'92*, vol. 2, Paris, France, 1992, pp. 637–641.
- [5] F. Caricchi, F. Crescimbin, E. Santini, and C. Santucci, "Influence of the radial variation of the magnet pitches in slotless PM axial flux motors," in *Proc. IEEE-IAS Annu. Meeting*, vol. 1, 1997, pp. 18–23.
- [6] F. Caricchi, F. Crescimbin, O. Honorati, G. L. Bianco, and E. Santini, "Performance of core-less winding axial-flux PM generator with power output at 400 Hz-3000 rev/min.," *IEEE Trans. Ind. Appl.*, vol. 34, no. 6, pp. 1263–1269, Nov./Dec. 1998.
- [7] F. Caricchi, F. Crescimbin, E. Santini, and C. Santucci, "FEM evaluation of performance of axial flux slotted PM machines," in *Proc. IEEE-IAS Annu. Meeting*, vol. 1, 1998, pp. 12–18.
- [8] G. W. Carter, *Electromagnetic Field in Its Engineering Aspects*. London, U.K.: Longmans, 1954.
- [9] W. S. Leung and C. C. Chan, "A new design approach for axial field electrical machine," *IEEE Trans. Power. App. Syst.*, vol. PAS-99, no. 4, pp. 1679–1685, 1980.
- [10] C. C. Chan, "Axial-field electrical machines: Design and application," *IEEE Trans. Energy Convers.*, vol. 2, no. 2, pp. 294–300, Jun. 1987.
- [11] J. Engstrom, "Inductance of slotless machines," in *Proc. IEEE Nordic Workshop on Power and Industrial Electronics*, Aalborg, Denmark, June 2000.
- [12] A. E. Fitzgerald and C. Kingsley, *Electric Machinery*, 2nd ed. New York: McGraw-Hill, 1961.
- [13] J. F. Gieras, R. Wang, and M. J. Kamper, *Axial Flux Permanent Magnet Brushless Machines*. Dordrecht, The Netherlands: Kluwer, 2004.
- [14] J. F. Gieras and M. Wing, *Permanent Magnet Motor Technology: Design and Applications*, 2nd ed. New York: Marcel Dekker, 2002.
- [15] C. Gu, W. Wu, and K. Shao, "Magnetic field analysis and optimal design of DC permanent magnet coreless disk machine," *IEEE Trans. Magn.*, vol. 30, no. 5, pp. 3668–3671, Sep. 1994.
- [16] V. B. Honsinger, "Performance of polyphase permanent magnet machines," *IEEE Trans. Power App. Syst.*, vol. PAS-99, no. 4, pp. 1510–1516, 1980.
- [17] A. Hughes and T. J. Miller, "Analysis of fields and inductances in air-cored and iron-cored synchronous machines," *Proc. Inst. Elect. Eng.*, vol. 124, no. 2, pp. 121–126, Feb. 1977.
- [18] M. J. Kamper, F. S. Van der Merwe, and S. Williamson, "Direct finite element design optimization of cageless reluctance synchronous machine," *IEEE Trans. Energy Convers.*, vol. 11, no. 3, pp. 547–555, Sep. 1996.
- [19] N. F. Lombard and M. J. Kamper, "Analysis and performance of an iron-less stator axial flux PM machine," *IEEE Trans. Energy Convers.*, vol. 14, no. 4, pp. 1051–1056, Dec. 1999.
- [20] H. C. Lovatt, V. S. Ramden, and B. C. Mecrow, "Design an in-wheel motor for a solar-powered electric vehicle," *Proc. Inst. Elect. Eng.—Elect. Power Appl.*, vol. 145, no. 5, pp. 402–408, 1998.
- [21] D. Mbidi, K. vd Westhuizen, R. Wang, M. J. Kamper, and J. Blom, "Mechanical design considerations of double stage axial-flux permanent magnet machine," in *Proc. IEEE-IAS 35th Annu. Meeting*, vol. 1, Rome, Italy, 2000, pp. 198–201.
- [22] M. J. D. Powell, "An efficient method for finding the minimum of a function of several variables without calculating derivatives," *Comput. J.*, vol. 7, pp. 155–162, 1964.
- [23] J. Saari and A. Arkkio, "Losses in high-speed asynchronous motors," in *Proc. IECM'94*, vol. 3, Paris, France, 1994, pp. 704–708.
- [24] R. Wang and M. J. Kamper, "Calculation of eddy current loss in axial field permanent magnet machine with coreless stator," *IEEE Trans. Energy Convers.*, vol. 19, no. 3, pp. 532–538, Sep. 2004.
- [25] R. Wang, M. J. Kamper, and R. T. Dobson, "Development of a thermo-fluid model for axial field permanent magnet machines," *IEEE Trans. Energy Convers.*, to be published.
- [26] R. Wang, "Design aspects and optimization of an AFPM machine with an ironless stator," Ph.D. dissertation, Dept. Elect. Eng., Univ. Stellenbosch, Matieland, South Africa, 2003.
- [27] R. Wang, H. Mohellebi, T. J. Flack, M. J. Kamper, J. Buys, and M. Felichi, "Two-dimensional Cartesian air-gap element (CAGE) for dynamic finite-element modeling of electrical machines with a flat air-gap," *IEEE Trans. Magn.*, vol. 38, no. 2, pp. 1357–1360, Mar. 2002.
- [28] S. Williamson and J. Smith, "The application of minimization algorithms in electrical engineering," *Proc. Inst. Elect. Eng. A*, vol. 127, no. 8, pp. 528–530, 1980.